On the measurement of ^{15}N–{^{1}H} nuclear Overhauser effects

Fabien Ferrage [a,b,*], Andrea Piserchio [a,c], David Cowburn [a], Ranajeet Ghose [c,d]

[a] New York Structural Biology Center, 89 Convent Avenue, Park Building at 133rd Street, New York, NY 10027, USA
[b] Département de Chimie, Ecole Normale Supérieure, C.N.R.S. U.M.R. 8642; 24 rue Lhomond, 75231 Paris cedex 05, France
[c] Department of Chemistry, City College of the City University of New York, NY 10031, USA
[d] Graduate Center of the City University of New York, NY 10016, USA

ABSTRACT

Accurate quantification of the ^{15}N–{^{1}H} steady-state NOE is central to current methods for the elucidation of protein backbone dynamics on the fast, sub-nanosecond time scale. This experiment is highly susceptible to systematic errors arising from multiple sources. The nature of these errors and their effects on the determined NOE ratio is evaluated by a detailed analysis of the spin dynamics during the pair of experiments used to measure this ratio and possible improvements suggested. The experiment that includes ^{1}H irradiation, is analyzed in the framework of Average Liouvillian Theory and a modified saturation scheme that generates a stable steady-state and eliminates the need to completely saturate ^{1}H nuclei is presented. The largest source of error, however, in ^{1}H-dilute systems at ultra-high fields is found to be an overestimation of the steady-state NOE value as a consequence of the incomplete equilibration of the magnetization in the so-called "reference experiment". The use of very long relaxation delays is usually an effective, but time consuming, solution. Here, we introduce an alternative reference experiment, designed for larger, deuterated systems, that uses the fastest relaxing component of the longitudinal magnetization as a closer approximation to the equilibrium state for shorter relaxation delays. The utility of the modified approach is illustrated through simulations on realistic spin systems over a wide range of time scales and experimentally verified using a perdeuterated sample of human ubiquitin.

© 2008 Elsevier Inc. All rights reserved.

1. Introduction

The ability to characterize protein dynamics at atomic resolution is key to understand biological processes, such as enzymatic reactions, protein folding, the driving forces of interactions and allostery. Nuclear magnetic resonance (NMR) is a powerful tool to study protein dynamics over a wide range of time scales [1,2]. Hydrodynamic properties of proteins in solution and dynamics occurring faster than a few nanoseconds are usually measured by the quantitative analysis of ^{15}N relaxation rates [2–5]. These rates depend both on the overall rotational diffusion in solution as well as fast backbone motions on a sub-nanosecond time scale through their effects on the spectral density functions [6–9]. Longitudinal and transverse relaxation rates largely sample the spectral density at low (^{15}N Larmor frequency) and zero-frequency [6,7]. The accurate determination of the spectral density function at high frequencies (around the ^{1}H Larmor frequency)

relies on the accurate measurement of ^{15}N–{^{1}H} nuclear Overhauser effects (NOE) [10].

Several studies have underlined the effect on the measured value of the steady-state ^{15}N–{^{1}H} NOE of incomplete relaxation to the steady-state, or equilibrium, ^{15}N polarization in the pair of experiments with and without (reference) ^{1}H saturation [11–13]. Ways to accelerate the evolution towards the equilibrium polarization have been found [11] and correction factors introduced [14]. However, Gong and Ishima [12] have recently shown that, on high-field spectrometers and particularly using highly deuterated proteins, cross-relaxation pathways due to the cross-correlation of chemical shift anisotropy (CSA) and dipole–dipole (DD) interactions could significantly slow down the recovery of equilibrium polarization. A simple way to overcome this problem is to introduce a longer relaxation delay in the reference experiment. This solution is simple to implement and is recommended for small, deuterated proteins. However, it is extremely time-consuming since durations larger than 10 s should be employed.

In this article, we introduce two modifications to commonly employed pulse sequences to reduce potential artifacts. These modifications are based on our theoretical treatment of the experiments. We first present a theoretical framework for the detailed analysis of spin dynamics during the course of the steady-state

* Corresponding author. Address: Département de Chimie, Ecole Normale Supérieure, C.N.R.S. U.M.R. 8642; 24 rue Lhomond, 75231 Paris cedex 05, France. Fax: +1 33 1 44 32 33 97.
E-mail address: Fabien.Ferrage@ens.fr (F. Ferrage).

^{15}N–{^{1}H} NOE experiment using a realistic spin system. Then, we analyze the saturated experiment in the framework of Average Liouvillian Theory [15,16]. We evaluate the effects of the sequence of pulses and delays in the saturation block and provide suggestions to reduce sources of errors in the measured steady-state NOE value. We examine the non-saturated experiment next and introduce a simple and effective modification to commonly employed sequences which accelerate recovery towards equilibrium. The use of this sequence is recommended for larger, deuterated proteins. The improvements in accuracy resulting from the new sequences set (saturated and reference) are evaluated on a sample of perdeuterated human ubiquitin at high-fields (16.5 T and 21.1 T).

2. Theory

2.1. Definitions

For cases where the polarization does not evolve towards an effective zero steady-state [17], the homogeneous master equation (HME) [15,16,18] provides the most convenient theoretical framework to describe longitudinal relaxation. For instance, Di Bari and Levitt [15] have shown that it was possible to create several kinds of steady-state terms under multiple-pulse experiments. These results are described elegantly and efficiently in the framework of Average Liouvillian Theory [15,16]. Using the notation of Ghose [16], one can write the HME:

$$\frac{d\sigma(t)}{dt} = -\widehat{L}(t)\sigma(t), \tag{1}$$

where σ is the density operator and $\widehat{L}(t)$ the Liouvillian superoperator, defined as:

$$\widehat{L}(t) = i\widehat{H}(t) + \widehat{\Gamma}(t) + \widehat{\Theta}(t). \tag{2}$$

$\widehat{H}(t)$ is the Hamiltonian superoperator that contains all coherent terms, $\widehat{\Gamma}(t)$ is the relaxation superoperator that accounts for the non-coherent evolution towards the steady-state, and $\widehat{\Theta}(t)$ is the thermal correction superoperator. The steady-state represents the state of thermal equilibrium in the absence of any significant perturbations to the Zeeman interactions.

In the present context, we treat coherent evolutions under radio-frequency (RF) fields as perfect instantaneous rotations, allowing the Liouvillian superoperators to be simplified to include only relaxation and thermal correction terms. All the relevant spin dynamics can then be analyzed using a simple 4-dimensional Liouville space for a two-spin system in the basis $\{E/2, N_z, H_z, 2N_zH_z\}$, where E is the identity operator. The Liouvillian superoperator, for an amide ^{1}H, ^{15}N spin pair can be written as:

$$\widehat{L} = \begin{pmatrix} 0 & 0 & 0 & 0 \\ \theta_N & \rho_N & \sigma_{NH} & \delta_N \\ \theta_H & \sigma_{NH} & \rho_H & \delta_H \\ \theta_{NH} & \delta_N & \delta_H & \rho_{NH} \end{pmatrix} \tag{3}$$

where ρ_N is the longitudinal relaxation rate of the ^{15}N nucleus, ρ_H is the longitudinal relaxation rate of ^{1}H, ρ_{NH} is the auto-relaxation rate of the two-spin order, σ_{NH} is the auto-correlated dipolar cross-relaxation rate, δ_N (or δ_H) is the longitudinal cross-relaxation rate due to the cross-correlation of the ^{15}N (or ^{1}H) chemical shift anisotropy (CSA) and the ^{15}N–^{1}H dipole–dipole (DD) interaction. If one normalizes [19] the equilibrium ^{15}N polarization to be 1, thermal correction terms can be written as:

$$\begin{aligned} \theta_N &= \rho_N + \frac{\gamma_H}{\gamma_N}\sigma_{NH} \\ \theta_H &= \sigma_{NH} + \frac{\gamma_H}{\gamma_N}\rho_H \\ \theta_{NH} &= \delta_N + \frac{\gamma_H}{\gamma_N}\delta_H \end{aligned} \tag{4}$$

2.2. Symmetry of the saturation block

The experimental scheme often employed for ^{1}H saturation while observing the steady-state on ^{15}N is depicted in Fig. 1a. The pulse applied on ^{1}H is often a $2\pi/3$ rotation, however, we will consider π rotations in this discussion for simplicity and this leads to no loss of generality. An alternative symmetric saturation scheme is presented in Fig. 1c. The scheme of Fig. 1b is a formally identical expansion of the scheme of Fig. 1a, and the schemes of Fig. 1d and c are similarly identical. The average Liouvillian that describes the evolution of the density operator during the bracketed element of Fig. 1b and d is given by:

$$\widehat{L}_{av} = \widehat{L}_{av}^{(0)} + \widehat{L}_{av}^{(2)} + \ldots \tag{5}$$

with:

$$\widehat{L}_{av}^{(0)} = \frac{1}{2}(\widehat{L} + \widehat{R}\widehat{L}\widehat{R}^{-1}) = \begin{pmatrix} 0 & 0 & 0 & 0 \\ \theta_N & \rho_N & 0 & 0 \\ 0 & 0 & \rho_H & \delta_H \\ 0 & 0 & \delta_H & \rho_{NH} \end{pmatrix} \tag{6}$$

where $\widehat{R}$ represents the inversion due to a π ^{1}H pulse:

$$\widehat{R} = \begin{pmatrix} 1 & 0 & 0 & 0 \\ 0 & 1 & 0 & 0 \\ 0 & 0 & -1 & 0 \\ 0 & 0 & 0 & -1 \end{pmatrix} \tag{7}$$

Note that all odd-order terms in the average Liouvillian vanish, because the bracketed sequences (Fig. 1b and d) are symmetric. The subspace of odd terms, consisting of operators inverted by π ^{1}H pulses (i.e. H_z and $2N_zH_z$) is decoupled from the even subspace consisting of operators invariant under ^{1}H pulses (i.e. $E/2$ and N_z). $\widehat{L}_{av}^{(0)}$ leads to a mono-exponential evolution of ^{15}N longitudinal polarization with a rate ρ_N towards the well-known steady-state polarization $\langle N_z^{ss} \rangle$:

$$\frac{\langle N_z^{ss} \rangle}{\langle N_z^{eq} \rangle} = 1 + \frac{\gamma_H}{\gamma_N}\frac{\sigma_{NH}}{\rho_N} \tag{8}$$

where $\langle N_z^{eq} \rangle$ is the equilibrium polarization of the ^{15}N nucleus.

All higher order terms in the average Liouvillian may be neglected when the inter-pulse delay 2τ is short. The steady-state described by Eq. (8) will be reached after an integer number of saturation elements. One can notice that a delay τ after the last multi-pulse element, in Fig. 1b, corresponding to one half of the inter-pulse delay is therefore not required and leads to an evolution of ^{15}N polarization away from the steady-state towards equilibrium. This effect is often negligible when the steady-state and equilibrium polarizations are comparable and typical values of τ that range from 2.5 to 10 ms are used. However, systematic errors up to a few percent may be found for mobile residues with negative NOE ratios (Eq. (8) i.e when $\left| \frac{\gamma_H}{\gamma_N}\frac{\sigma_{NH}}{\rho_N} \right| > 1$) and typical longitudi-
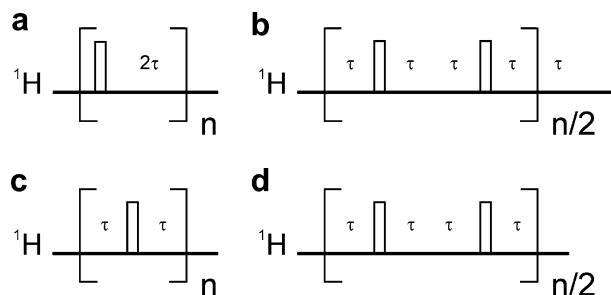
Fig. 1. Schematic representation of ^{1}H saturation elements to measure the steady-state polarization on the ^{15}N nucleus. (a and b) Two forms of a typical saturation sequence when π pulses are used on the ^{1}H. (c and d) Two forms of a symmetric saturation element.

nal relaxation rates of the order of 1 s^{-1}. It is therefore preferable that a symmetric saturation element like Fig. 1c be used, since no additional saturation period is required (in practical terms, an initial recovery delay is always employed to lock the magnetic field allowing the first delay τ to be deleted) but may suppress small systematic errors.

2.3. Is saturation of ^{1}H polarization necessary?

It is quite remarkable that the degree of saturation of the ^{1}H polarization does not appear in Eqs. (5)–(8). In fact, in an extreme case with no auto-relaxation of ^{1}H nuclei and perfect π pulses (i.e. no saturation), the system evolves exactly towards the steady-state polarization. Indeed, during every element of Fig. 1c and d, a ^{15}N nucleus sees its neighboring ^{1}H nucleus an equal amount of time as spin-up and spin-down. Thus, on average, the ^{1}H polarization appears saturated to the ^{15}N nucleus.

If the rate of pulsing on ^{1}H is fast, the evolution of the ^{1}H polarization during the inter-pulse (2τ) delay is very small. Therefore, during each saturation element, the ^{15}N nucleus sees also, on average, a saturated ^{1}H nucleus. There is thus no requirement for the ^{1}H polarization to be saturated. In all simulations displayed in Fig. 2, the residual polarization of ^{1}H is still larger than 5% of the equilibrium polarization after 5 s. Nevertheless, the ^{15}N polarization is identically equal to the expected steady-state polarization when the inter-pulse delay (2τ) is short.

When the ^{1}H polarization is allowed to relax significantly towards equilibrium during the inter-pulse delay, the situation is more complex. On average, the polarization of ^{1}H is different from zero and the ^{15}N polarization does not evolve towards the "true" steady-state. Fig. 2 illustrates this property. For both a mobile NH pair and a rigid one, a delay τ as long as 50 ms is only marginally detrimental to the accuracy of the steady-state shown in Eq. (8). If one uses a symmetric saturation scheme, as depicted in the inserts in Fig. 2, the result is perfectly accurate. In the case of very long inter-pulse delays, the polarization of the steady-state is different from the one expected from Eq. (8). In the latter case, the ^{1}H polarizations are closer to equilibrium before each pulse on ^{1}H, so that, after the π pulse, the nitrogen polarization is driven towards $-\langle N_z \rangle^{eq}$. After half an inter-pulse delay, the system is still biased towards this state so that if the NOE ratio (Eq. (8)) is larger than -1, the nitrogen longitudinal polarization expectation value is smaller than the steady-state (Fig. 2). If the NOE ratio is smaller than -1, the expectation value is larger than the steady-state polarization (data not shown). One should notice that, under the conditions of the simulations, the system is significantly closer to the expected steady-state after half an inter-pulse delay, validating the use of a symmetric saturation scheme.

Our simulations clearly show that the saturation of ^{1}H polarization is not necessary if one chooses the proper symmetry properties for the saturation element. However, when one uses an asymmetric saturation scheme, the saturation of the ^{1}H polarization may become necessary. Indeed, if the saturation is complete, the expectation value of operators inverted by the pulses on ^{1}H is null: the longitudinal polarization of ^{1}H and the two-spin order polarization are zero. Therefore:
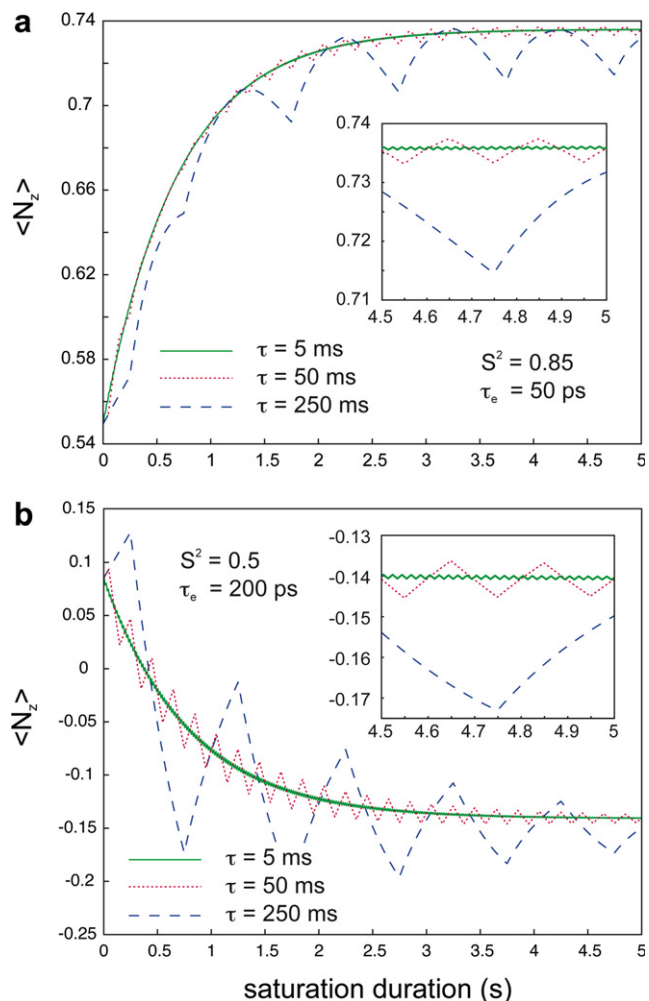
$$\widehat{R}^{-1}\sigma^{ss} = \sigma^{ss}, \tag{9}$$

where σ^{ss} is the density operator at the steady-state. From Eqs. (6) and (9), it follows that:

$$\overline{N}_z^T L \sigma^{ss} = \overline{N}_z^T L_{av}^{(0)} \sigma^{ss} = 0. \tag{10}$$

where $\overline{N}_z^T$ is the conjugate transpose of N_z. From Eqs. (1) and (10), one obtains:

$$\frac{d\langle N_z \rangle(t)}{dt}\bigg|_{t=0} = 0. \tag{11}$$

Fig. 2. Evolution of the ^{15}N longitudinal polarization towards the steady-state under the application of the saturation sequence of Fig. 1c with different values for the delay τ. For a rigid system (a), the Lipari–Szabo [20] form of the spectral density function was used with an order parameter S^2 equal to 0.85 and the correlation time for local motions was 50 ps. For a mobile residue (b), the order parameter was 0.5 and the local correlation time was 200 ps. The inserts show the details of the last 500 ms of this evolution. As in the experimental situations, the system is allowed to relax from a fully saturated state for two seconds before the beginning of the saturation scheme. A small spherical deuterated protein was taken as an example: a single global rotation correlation time of 4.5 ns was used and the ^{15}N–^{1}H pair was supplemented with two ^{1}H nuclei located at 290 pm of the ^{15}N bound ^{1}H. The relaxation superoperator used for this calculation is displayed in the Appendix.

The initial slope for the evolution of the longitudinal polarization of the ^{15}N nucleus is zero.

In the case where the ^{1}H polarization is fully saturated, i.e. the ^{1}H polarization is zero, schemes presented in Fig. 1a and c will provide identical expectation values for the longitudinal polarization of the ^{15}N nucleus unless the delay τ is much longer than values typically employed in experiments (5–10 ms). The outcome of these two schemes will only be different in fast-relaxing systems (i.e. when τ is comparable to the relaxation rates) or when the ^{1}H and two-spin order polarizations are significantly different from zero.

Nevertheless, complete saturation of the polarization of ^{1}H may be difficult to achieve [13], particularly in cases where cross-relaxation or exchange with the slow-relaxing ^{1}H nuclei from the solvent is efficient. By reducing the need for saturation of the ^{1}H nuclei, the use of a symmetric saturation scheme, which comes at no cost, reduces one source of systematic errors. Even though the benefits may be limited is most cases, its use is recommended.

2.4. Relaxation in the reference experiment

As discussed in Section 2.2, the effective relaxation of the ^{15}N longitudinal polarization during the saturation scheme is a mono-exponential evolution towards the steady-state. Relaxation during the reference experiment is much more complex.

As shown in the Redfield theory of relaxation [8], the secular approximation suppresses many of the possible cross-relaxation pathways. All longitudinal operators commute with the Zeeman and scalar coupling Hamiltonian operators. Therefore, in the absence of radio-frequency fields, all possible cross-relaxation path-ways are active in the relevant Liouville subspace. The consequence is that relaxation towards equilibrium is potentially highly multi-exponential. As shown by Gong and Ishima [12], when small, highly deuterated proteins are under study at high-fields, dipole–dipole/CSA cross-correlated cross-relaxation [21] is sufficient to lead to a very slow evolution towards equilibrium for the ^{15}N longitudinal polarization. In larger non-deuterated proteins, the lifetime of the two-spin order $2H_zN_z$ is short, which significantly reduces this effect.

Nevertheless, deuterated proteins are excellent tools for relaxation studies, e.g. when basic ^{15}N relaxation experiments are sup-
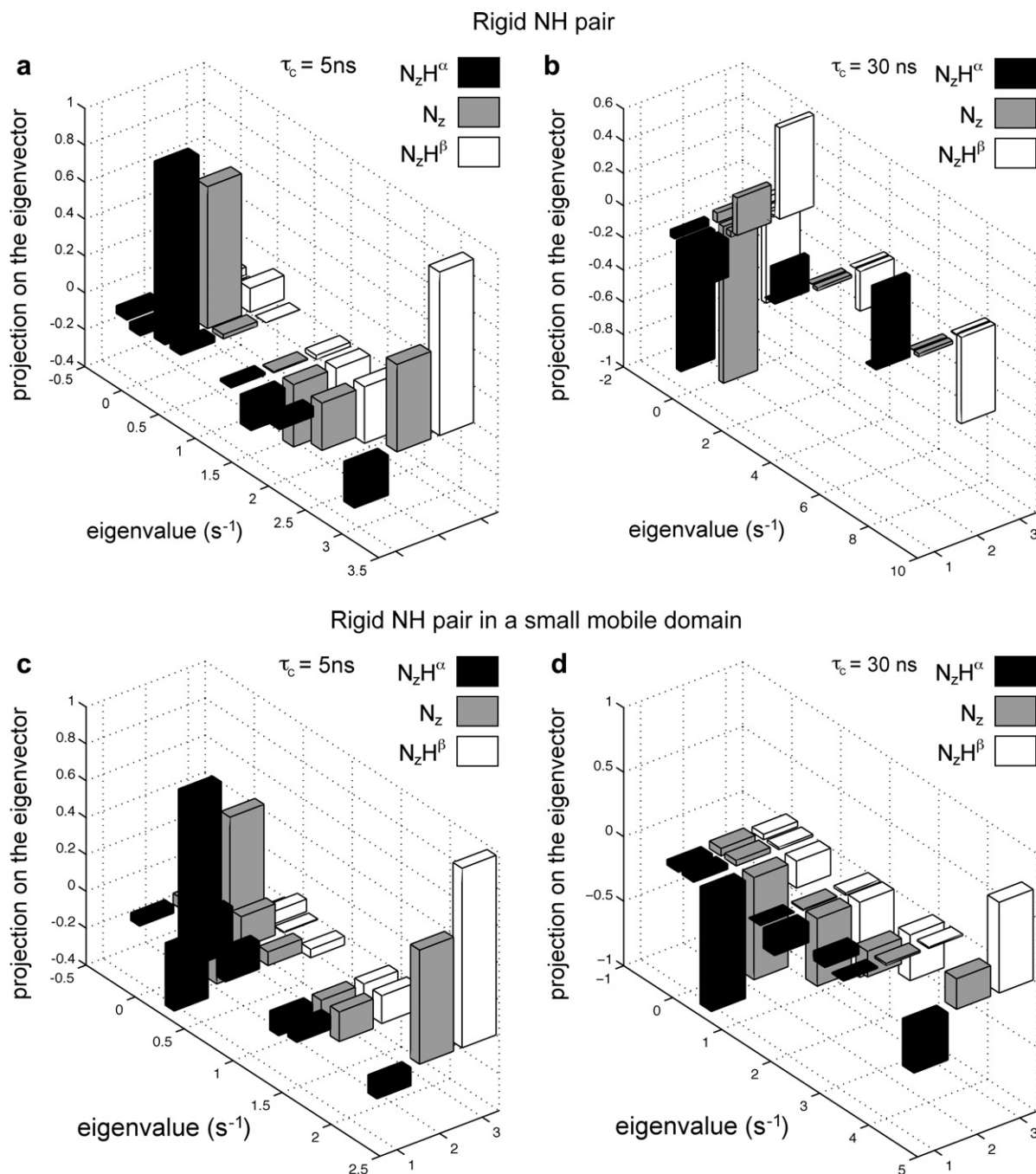
Fig. 3. Projection of the accessible observables $2H^\beta N_z$ $2H^\alpha N_z$ and N_z on the eigenvectors of the Liouvillian superoperator that governs the evolution towards equilibrium. Eigenvalues are reported on the x-axis while the projections of the observables on the corresponding eigenvectors are reported on the z-axis. (a and b) For a rigid group with the same parameters as those used in Fig. 2. (c and d) For a rigid group in a small mobile domain with the same parameters for local motions and a domain motion characterized by a correlation time equal to 10% of the overall tumbling time and an order parameter for slow motions of 0.3. The overall tumbling correlation time employed is (a and c) 5 ns and (b and d) 30 ns.

plemented by experiments where the ^{1}H polarization participates in the coherence being followed. For example, the characterization of chemical exchange parameters is significantly improved by the implementation of CPMG (Carr Purcell Meiboom Gill) schemes on amide ^{1}H [22,23], and the measurement of cross-relaxation under the cross-correlation of dipolar and CSA interactions to complement typical ^{15}N relaxation experiments allows an accurate determination of relaxation under chemical exchange [17,24]. The accuracy of the quantitative analyses of these experiments benefit strongly from deuteration. Thus in addition to large proteins, where the benefits of deuteration have been discussed at length elsewhere [25] and its application to relaxation studies demonstrated [26–28], deuteration of small proteins is also greatly beneficial especially when detailed, quantitative analyses are required to interpret data from relaxation experiments.

An accurate method to measure ^{15}N–{^{1}H} nuclear Overhauser effects adapted for deuterated proteins at high-fields is, to the best of our knowledge, not available in the literature. A difficulty here is that manipulations of the spin system designed to alter cross-relaxation pathways would make the effective final state of the system different from the equilibrium state. In the absence of any manipulation of the spin system, it is still possible to accelerate the evolution towards equilibrium by an appropriate choice of the operator being followed. Indeed, the closer this operator is to the fastest relaxing relaxation modes of the density operator, the more efficient is its evolution towards equilibrium.

The development of spin-state-selective experiments [29–32] has made the manipulation of single-transition operators very convenient. Fig. 3 compares the projections of three longitudinal operators that can be readily converted to observables: the longitudinal polarization of the ^{15}N nucleus and the two single-transition longitudinal operators. The spin system employed for this calculation comprises additional protons (see Appendix), so that there are eight eigenvalues and not four, as expected from Eq. (3). It is quite remarkable that, for a rigid NH pair in a small protein (overall correlation time 5 ns) with a magnetic field of 21.1 T, the two single-transition operators are very close to either the slowest relaxing mode or the fastest relaxing mode of the spin system, as can be seen in Fig. 5a. This is because the dominant contributions to relaxation rates are the ^{15}N–^{1}H dipole–dipole and ^{15}N CSA, while the static field is close to its optimal value for relaxation interference [33]. This makes of the fast-relaxing single-transition operator $2N_zH^\beta$ the ideal operator to be followed in an experiment designed to reduce the recovery delay. In this study, we will refer to $2N_zH^\beta$ as the fast-relaxing single-transition. This is consistent with the definitions of relaxation rates provided in the Appendix but may be in contradiction with part of the literature on the subject.

In a rigid NH pair in a large protein (Fig. 3b), however, the longitudinal polarization of the ^{15}N nucleus is almost equal to the eigenvector with the lowest non-zero eigenvalue. The projections on fast-relaxing modes are only slightly larger for the $2N_zH^\beta$ operator. In this case, ^{1}H–^{1}H cross-relaxation is the dominant mechanism for relaxation. One consequence is the effective decoupling of CSA/DD cross-relaxation pathways. If semi-local motions, such as small-domain motions, occur on an intermediate time scale (this assumes that the fast sub-nanosecond motions occur on two different time scales that differ by at least one order of magnitude), the projection of $2N_zH^\beta$ on fast-relaxing modes increases significantly (Fig. 3d), so that this operator is, again, the most relevant "observable". Overall, Fig. 3 shows that this operator should relax faster than the other accessible operators.

To confirm this trend, we have simulated the evolution towards equilibrium of all three operators under three classes of local dynamics and over a wide range of overall tumbling times. Results are displayed in Fig. 4 while the calculated rates are plotted in Fig. 5. As illustrated by the bold line in all simulations, the same
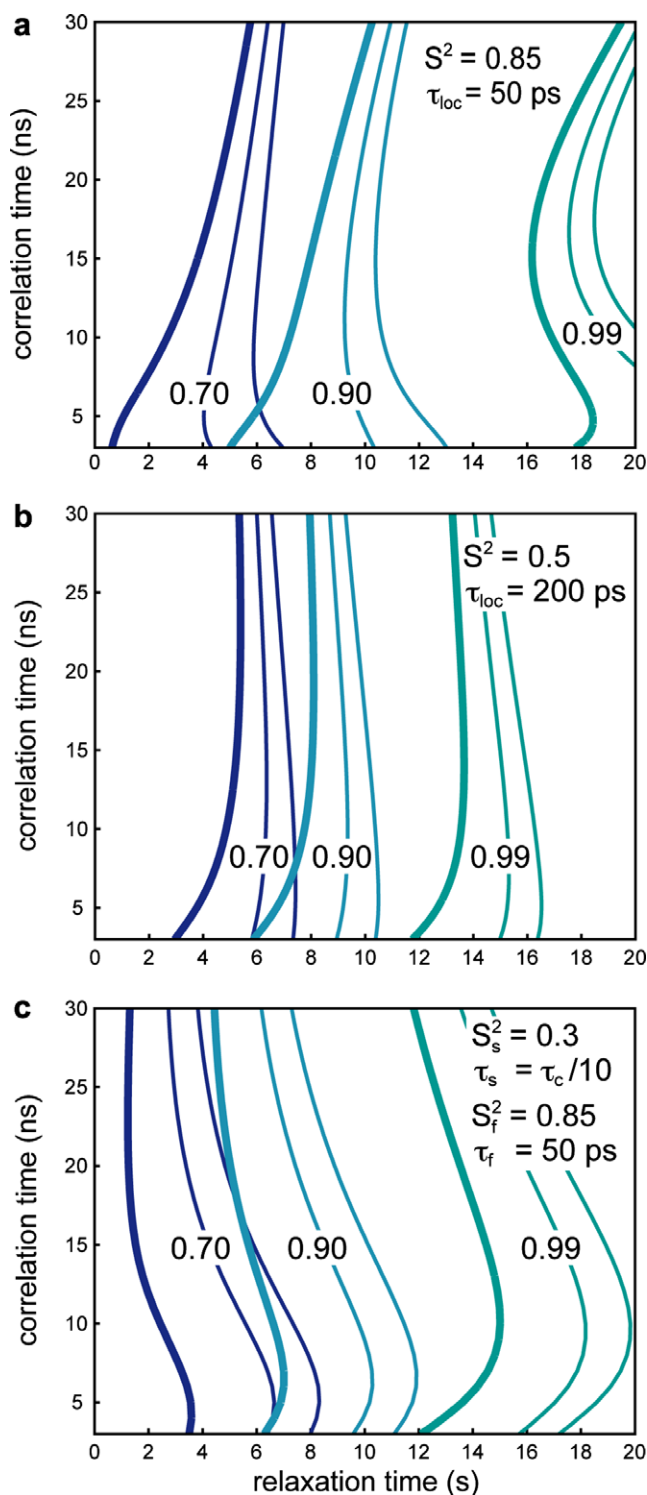
Fig. 4. Evolution of ^{15}N longitudinal polarization operators towards equilibrium from a fully saturated state. The bold contour lines correspond to the expectation value $\langle 2H^\beta N_z \rangle$. The thin line that carries the labels corresponds to the expectation value $\langle N_z \rangle$ while the second thin line represents the expectation value $\langle 2H^\alpha N_z \rangle$. The parameters for local dynamics are displayed on each figure. They correspond to (a) a rigid NH pair, (b) a mobile NH pair and (c) a rigid NH pair in a mobile domain. Contour lines are plotted for a polarization equal to 70% (blue); 90% (cyan); and 99% (green) of its equilibrium value.

single-transition is the closest to equilibrium, under all simulated circumstances and all times. In small proteins, the advantage is dramatic. In larger systems, the difference between the relaxation properties of the three operators for rigid NH pairs (as illustrated
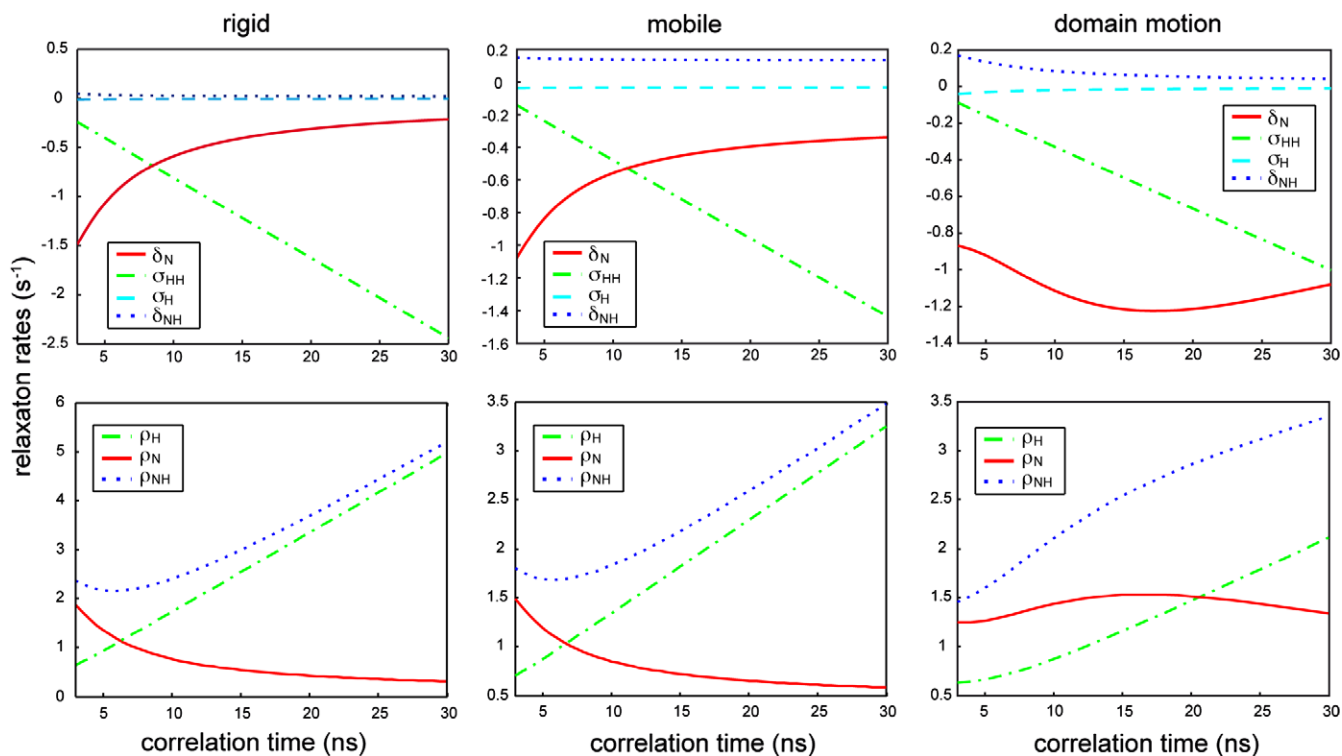
Fig. 5. Relaxation rates calculated for the simulations displayed in Fig. 4. See the appendix for detailed expressions of the rates.

by Fig. 3b) and very mobile NH pairs becomes smaller, as expected from Fig. 3. Fig. 5 illustrates the dominance of ^{1}H–^{1}H dipolar cross-relaxation in this regime. However, in the presence of small-domain motions the quantification of the operator $2N_zH^\beta$, provides a much closer estimate of the equilibrium polarization because it relaxes at a significantly faster rate than the other two operators over the entire range of overall tumbling times explored.

For example, in a large deuterated protein with an overall tumbling time of 20 ns, for which the use of this pulse sequence is recommended, we predict that, in a rigid system ($S^2 = 0.85$ and $\tau_{loc} = 50$ ps) studied on a 900 MHz spectrometer, 98% of the equilibrium polarization is recovered after 14 s for the fast-relaxing single-transition. For the same duration, 97.1% of the equilibrium longitudinal ^{15}N polarization is recovered, while 98% would be obtained after 15.25 s. The difference for this system is not spectacular, but the reduction of 8% of the relaxation delay should be welcome.

Fig. 4 shows that, even if the advantage for the selection of one single-transition operator may be limited for specific cases, selection of this operator always leads to the closest estimate of equilibrium. Therefore, it should always be advisable to measure the polarization of the fast-relaxing longitudinal single-transition of the ^{15}N nucleus as a standard for equilibrium in the experiment without ^{1}H saturation when measuring the steady-state ^{15}N–{^{1}H} NOE with TROSY-based sequences.

3. Materials and methods

All simulations were performed using MATLAB (www.mathworks.com). The programs can be provided upon request and only a few major features are discussed here. The spin system considered comprised one ^{15}N nucleus and three ^{1}H nuclei. The distance between the ^{15}N nucleus and its bound ^{1}H nucleus is 102 pm. The distances between this ^{1}H nucleus and its two neighbors are both 290 pm ([30]). The ^{1}H–^{1}H cross-relaxation rate was added to the auto-relaxation rate of one of the two neighboring ^{1}H nuclei to take into account the effect of cross-relaxation or exchange with ^{1}H from the solvent. Values for the CSA of ^{1}H and ^{15}N nuclei are the average values provided by Loth et al. in their study of human ubiquitin [35]. The model-free form of the spectral density function was used to describe rigid and mobile residues [20]. The extended model-free form was employed to take into account small-domain motions [36]. The spectral density function was adapted to include cross-correlated relaxation as in Loth et al. [35].

We have designed a new reference experiment, shown in Fig. 6, where the element that suppresses all polarizations involving the ^{1}H nucleus [26,37] (the element between points A^{sat} and B^{sat} in the saturated experiment) is substituted by a conversion between the fast- and slow-relaxing components of the polarization. At point A^{ref}, after a relaxation delay with a total duration $T_{lock} + T$, the expectation value $\langle 2N_zH^\beta \rangle$ is larger than $\langle 2N_zH^\alpha \rangle$. A composite π pulse on the ^{1}H channel interconverts these two operators, so that, at point B^{ref} in the sequence, the expectation value for $2N_zH^\beta$ is closer to equilibrium. The latter operator is subsequently detected in a TROSY manner: a spin-state-selective transfer follows the ^{15}N frequency labeling for the detection of a TROSY-like spectrum [31]. The conversion between the polarizations is achieved by a composite π pulse on the ^{1}H channel to reduce effects of RF-field inhomogeneities flanked by two $\pi/2$ very selective pulses to ensure an efficient restoration of the water magnetization to the $+z$-axis.

All experiments were performed on Bruker Advance NMR spectrometers operating at ^{1}H Larmor frequencies of 500, 700 and 900 MHz equipped with TXI cryoprobes with z-axis gradients. A sample of perdeuterated, uniformly ^{15}N-labelled ubiquitin (0.5 mM, in 50 mM ammonium acetate, 300 mM NaCl, pH 4.8) was used for all experiments. R_1, R_2 and ^{15}N–{^{1}H} NOE values (using the experiment presented here with a $T_{lock} + T$ value of 8 s, 16 scans per transient) were obtained at 500 MHz. The
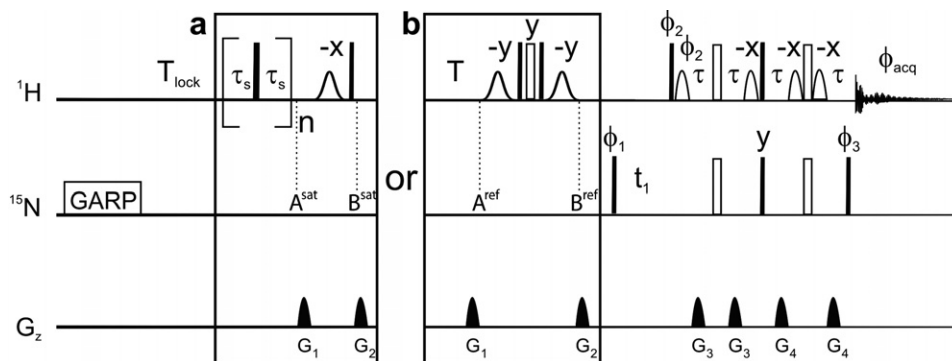
Fig. 6. Pulse sequences used for recording steady-state ^{15}N–$\{^1$H$\}$ nuclear Overhauser effects. In all experiments, a GARP [34] decoupling scheme was initially applied on the ^{15}N channel for 60 ms followed by a 2 s recovery delay (T_{lock}) used to lock the magnetic field. Saturated and reference experiments were run in an interleaved manner with the boxed schemes (a) and (b), respectively. (a) A train of $2\pi/3$ pulses was applied on the ^{1}H channel for 4 s with a delay τ_s equal to 5 ms. (b) A recovery delay T is followed by a composite pulse flanked by two water flip-back pulses to invert all ^{1}H polarizations but water ^{1}H. The total recovery delay is $T_{lock} + T$. For comparison with the initial scheme for the reference experiment, bracketed saturation elements were replaced by the delay T. A classic TROSY detection follows for all experiments. Except in the saturation element, all narrow (filled) and (wide) open rectangles represent $\pi/2$ and π pulses, respectively. Pulse phases are along the x-axis of the rotating frame unless otherwise mentioned. Gaussian-shaped pulses are 2 ms and have a Gaussian shape truncated at 1% of the maximal amplitude. A longer duration of 3 ms is recommended if greater selectivity is required. Bell-shaped pulses are sinebell shaped pulses, of 1 ms. The delay τ is 2.717 ms. The phase cycles are $\phi_1 = \{y;-y;-x;x\}$ used with $\phi_2 = \{y\}$ and $\phi_3 = \{x\}$; and $\phi_1 = \{-y;y;-x;x\}$ used with $\phi_2 = \{-y\}$ and $\phi_3 = \{-x\}$ alternated for every other free induction decay. The phase cycle for acquisition is $\phi_{acq} = \{x;-x;-y;y\}$. The duration of acquisition is 120 ms. For the indirect dimension, 75 complex points were recorded with a spectral width of 34 ppm.

following relaxation delays were used for the R_1 and R_2 experiments: R_1: 5 (×2), 20, 100 (×2), 300 and 600 ms; R_2: 1 (×2), 50, 100 (×2), 150, 250 ms. A relaxation delay of 2 s was used between scans in the R_1 and R_2 experiments and 8 scans were collected per transient. All experiments were performed at 25 °C. Analysis of the relaxation rates was performed in the usual way using the program DIFFTENS v2.0 [38] using an isotropic diffusion model and yielded a rotational correlation time of 4.48 ± 0.05 ns.

R_1, R_2 and ^{15}N–$\{^1$H$\}$ NOE ratio were simulated using standard expressions [36] for a ^{15}N–^{1}H two-spin system using standard parameters for several motional models described in the legend to Figs. 9 and 10. The "experimental" precisions of the R_1, R_2 and ^{15}N–$\{^1$H$\}$ NOE ratio were assumed to be 2.5%, 2.5% and 5%, respectively. The micro-dynamic parameters were obtained assuming an isotropic overall motion and fitting to the 8 different motional models described in detail elsewhere using the DYNAMICS package [39].

4. Results and discussion

4.1. Quantification of the equilibrium polarization in the reference experiment

The scheme of Zhu et al. [37] as modified by Chill et al. [26] was compared to our present scheme, with the new reference experiment. Data obtained on a spectrometer with a 700 MHz Larmor frequency for ^{1}H are displayed in Fig. 7. As can be seen from Fig. 7a, after 6 s of total recovery time neither the initial scheme nor the new one provide with an exact measurement of the polarization at equilibrium. However, the new scheme gives a closer estimate of the equilibrium polarization. For most NH pairs, the polarization is larger than 95% of the equilibrium polarization, assuming that the polarization is at equilibrium after a period of 12 s. For the initial scheme, many residues are still below 90% of the equilibrium polarization. Fig. 7b shows the NOE ratios derived from the two experimental approaches. As expected, ours provides smaller absolute values for the NOE ratio. This translates into larger values for the cross-relaxation rate σ_{NH} when the NOE ratio is positive and smaller values of σ_{NH} when the NOE ratio is negative (Fig. 7c and d).

Since for most residues the NOE ratio is close to one, according to Eq. (8), a small error in this ratio may translate into large relative errors in the value of σ_{NH}: for several residues, this cross-relaxation rate can be underestimated by a factor of 2 (Fig. 7d). For very mobile residues that display a negative NOE ratio, the error is marginally attenuated, which explains why the dramatic error in the estimate of the polarization at equilibrium for the NH pair of residue 76 translates to a comparable error for σ_{NH}. The NOE ratios displayed in Fig. 7b for residue 36 deserve comment. These large values are due to the underestimation of the intensity in all reference experiments. The ^{1}H signal of residue 36 is the closest to the water resonance, so that the ^{1}H polarization is affected by 2 ms Gaussian water flip-back pulses. Therefore, in the original scheme, the polarization of the two-spin order is not properly suppressed, so that the slowly relaxing component has a major contribution to the detected signal. In our present scheme, the inversion of the polarization of the two-spin order is also not perfect, so that both single-transition polarizations are partially mixed. With the use of the same selective water flip-back pulses; the scheme introduced in this article is significantly more robust to this artifact than the original scheme.

Fig. 8 presents experimental results obtained on a 900 MHz (^{1}H Larmor frequency) spectrometer. This high magnetic field provides a close to maximum interference effect between the ^{15}N CSA and ^{15}N–^{1}H dipolar interactions [33]. On average, our scheme provides a significantly larger intensity (i.e. closer to equilibrium) after a recovery delay as long as 8 s. The results depend significantly on the NH pair observed. Gly76 shows the most spectacular improvement, which can be linked to a high degree of flexibility. However, the preceding residues in the flexible C-terminal tail show very similar intensities in the two experiments, in spite of a large mobility.

At both fields, the scheme introduced in this paper provides a better estimate of the equilibrium polarization for almost all residues. The number of residues for which the initial scheme provides a higher intensity is small and the extent of the difference is generally negligible. According to our simulations (Fig. 4) this tendency is verified under all dynamic regimes and all molecular masses explored. It is therefore recommended to employ the new TROSY-based scheme presented in Fig. 6, with more selective water flip-back pulses (for instance 3 ms Gaussian-shaped pulses truncated at one percent of the maximum amplitude at high-fields).
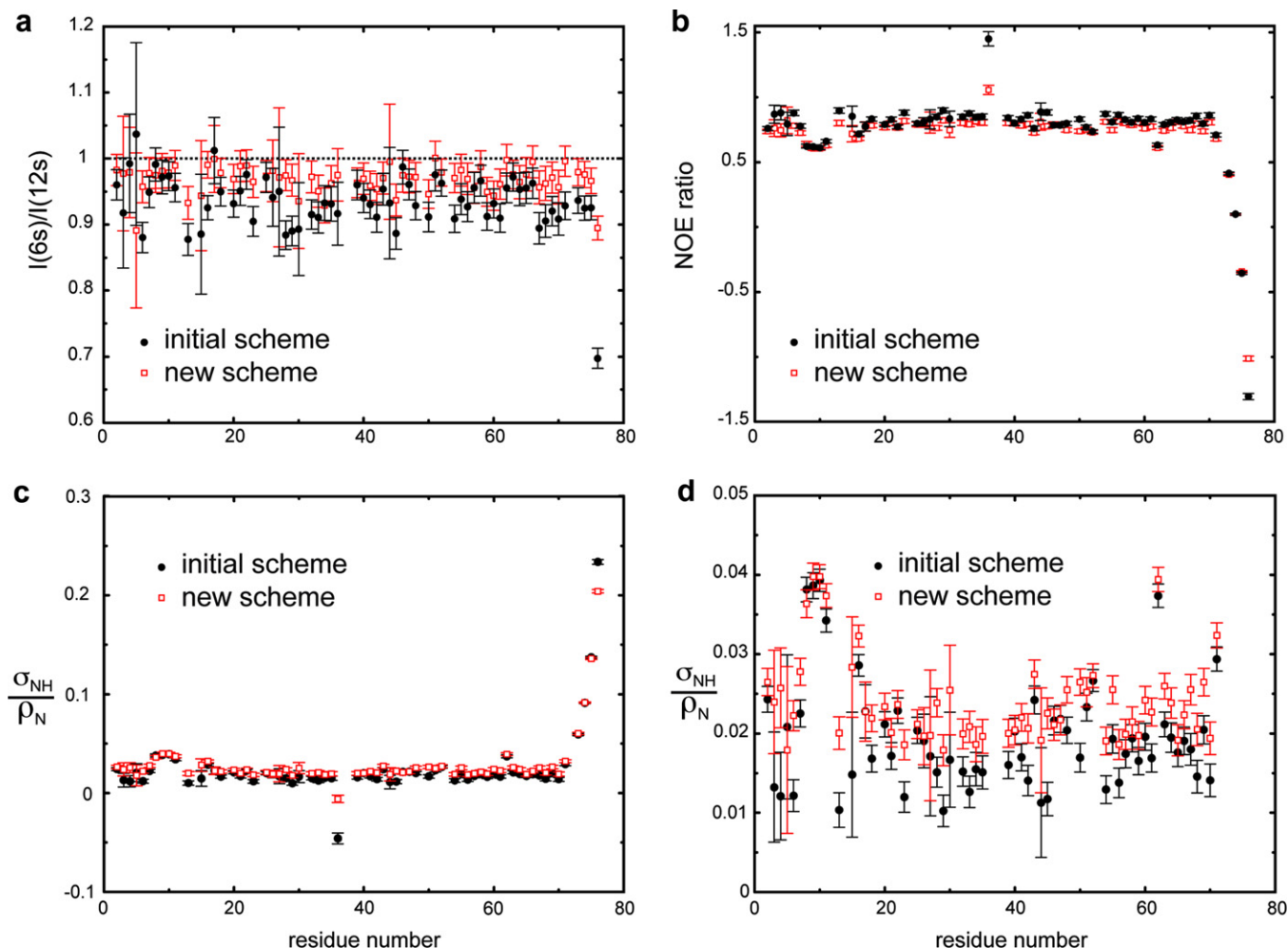
Fig. 7. Comparison of the initial and new schemes for the reference experiment at 16.4 T. (a) Ratio of intensities after a total of 6 s and 12 s of recovery. The delay is $T_{lock} + T$. T_{lock} is 2 s in all experiments. (b–d) The durations of the delay T and of the saturation schemes are both 4 s. (b) NOE ratio. (c) ratio of the dipolar cross-relaxation rates and longitudinal auto-relaxation rate of the ^{15}N nuclei derived from the NOE ratio of (b) as from Eq. (8). (d) Same as (c) with an expansion along the y-axis.
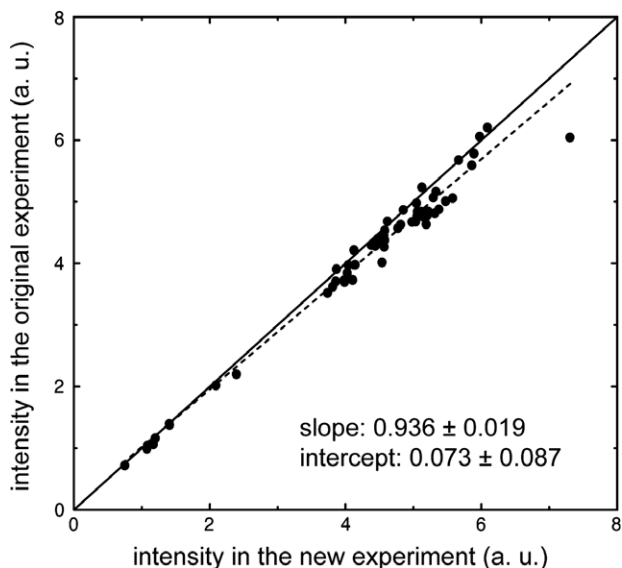

Fig. 8. Comparison of intensities of the experiment of Zhu et. al. [37] as modified by Chill et al. [26] and the new scheme. Error bars are smaller than the symbols. Experiments were recorded on a 900 MHz spectrometer with a total relaxation delay of 8 s. Results of a linear regression are shown by the dashed line.

Depending on the acquisition mode, the implementation of TROSY may lead to a loss of signal of a factor of 2 to $2\sqrt{2}$ if relaxation is negligible. ^{15}N–{^{1}H} NOE experiments are often signal-limited so that the use of TROSY for small proteins may not be the most appropriate method. It would indeed be more useful to employ twice longer relaxation recovery delays in the reference experiment with twice less scans and a conventional detection. That would lead to a good level of accuracy and more precision. On the other hand, if TROSY-based methods are to be used, which is the case for studies of large proteins or protein assemblies, the scheme discussed here should be favored.

4.2. Effect of the overestimation of the NOE on local dynamics parameters

The effect of the overestimation of ^{15}N–{^{1}H} NOE can lead to significant errors in the micro-dynamic parameters determined from an analysis of R_1, R_2 and ^{15}N–{^{1}H} NOE using the Lipari–Szabo or the extended Lipari–Szabo models. As seen in Fig. 9, for simple models, the overestimation has a profound effect on a rigid system with errors greater than 60% for the τ_e value even when the NOE value is overestimated by a mere 9% (Fig. 9c). When the overestimation is greater than 9%, the time scale of the local motion can
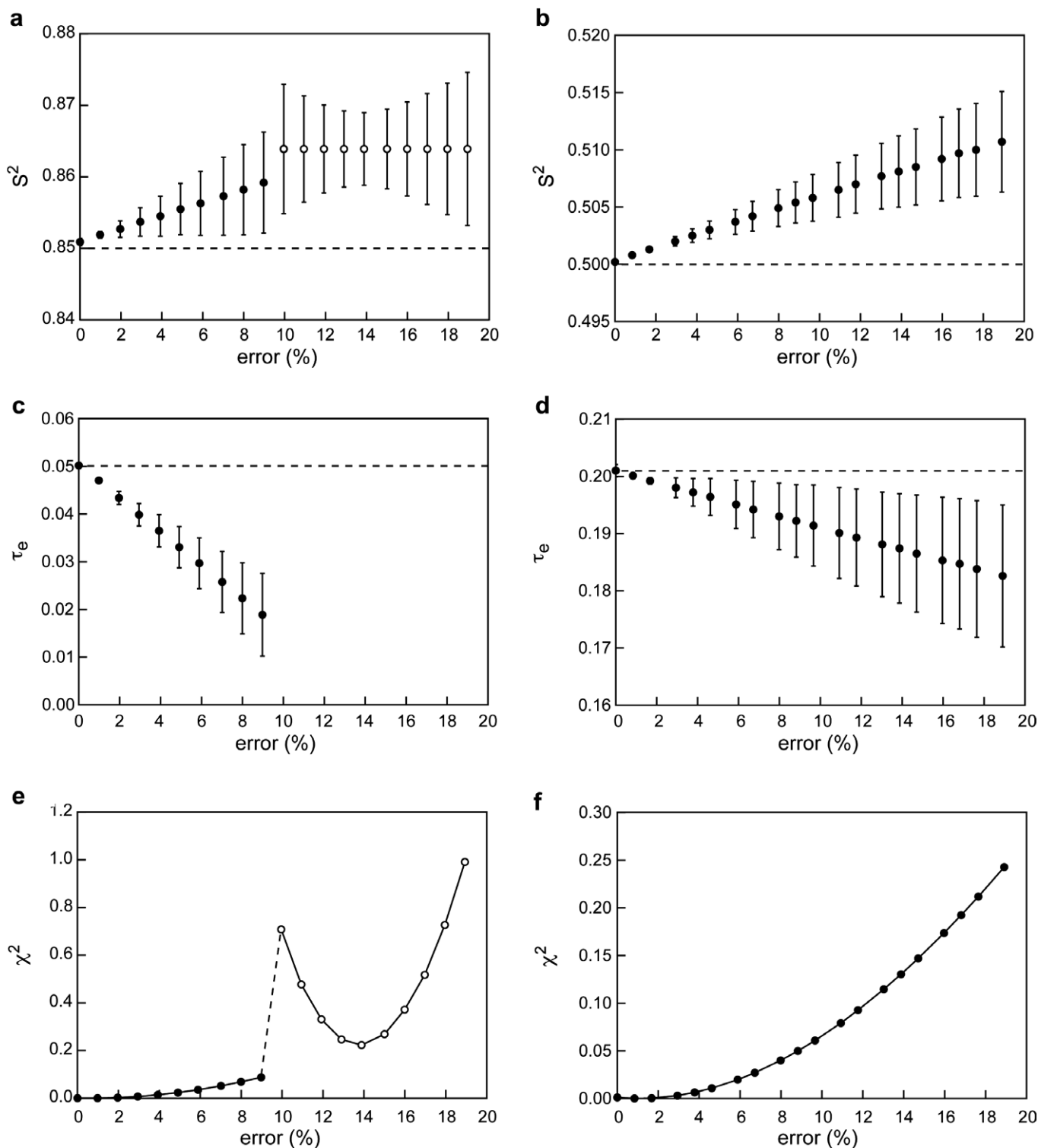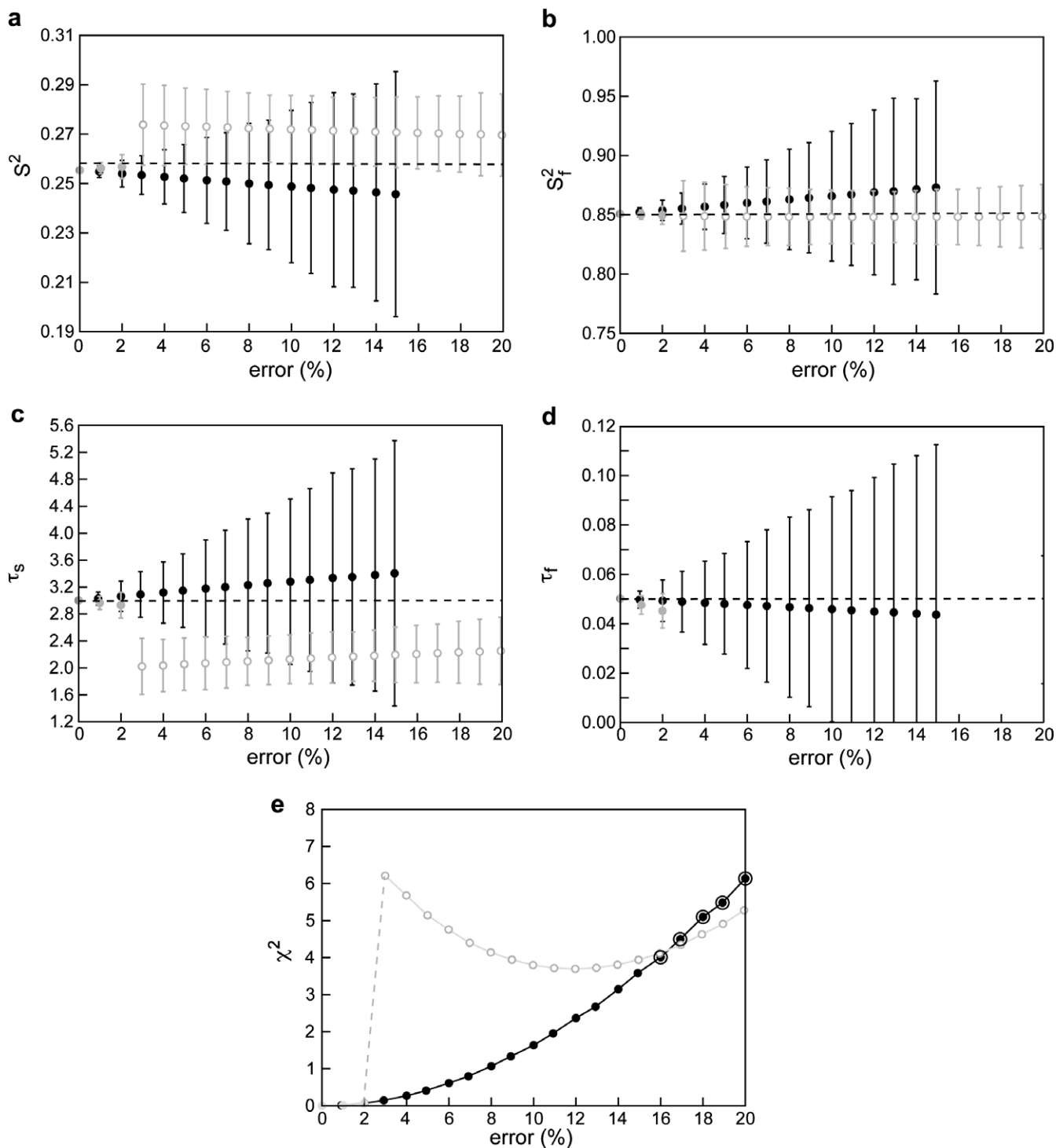
Fig. 9. Influence of overestimation of the ^{15}N–{^1H} NOE ratio on derived Lipari–Szabo micro-dynamic parameters. Parameters were obtained from theoretical R_1, R_2 and ^{15}N–{^1H} NOE ratio at 700 MHz assuming an overall correlation time of 4.5 ns, $S^2 = 0.85$ and $\tau_{loc} = 50$ ps (a,c,e) and $S^2 = 0.50$ and $\tau_{loc} = 200$ ps (b,d,f). "Experimental" errors of 2.5% for the R_1 and R_2 rates and 5% for the ^{15}N–{^1H} NOE were assumed. Filled circles represent cases where the correct (input) model (S^2, τ_{loc}) was selected based on the relaxation rates using a statistical F-test while open circles represent cases where the incorrect model (S^2 only) was chosen. The dashed lines (a–d) represent the correct motional parameters.

no longer be obtained and the incorrect motional model is selected based on a statistical F-test with very large increases in the χ^2 value (Fig. 9f). The effect is somewhat smaller in more dynamic systems. The transition point between different motional models being selected would necessarily depend on the software used to perform the Lipari–Szabo analysis and the particular algorithms utilized therein, however, the same general trends should be expected. The estimated S^2 values are less affected by the NOE overestimation with the errors being approximately 2% in both the rigid and dynamic cases. Additionally, when the NOE is overestimated, and

the degree of overestimation is much larger than the experimental precision (i.e. the random error in the experimental data), the complete set of relaxation data ceases to be self-consistent and large errors are obtained in the fitted micro-dynamic parameters for the same level of experimental precision. The magnitude of these errors become larger when more complex motional models are

Fig. 10. Influence of overestimation of the ^{15}N–{^{1}H} NOE ratio on Lipari–Szabo micro-dynamic parameters for a small rigid domain in a large protein. Parameters were obtained from theoretical R_1, R_2 and ^{15}N–{^{1}H} NOE ratio at 700 and 900 MHz (analyzed simultaneously) assuming an overall correlation time of 30 ns, $S_f^2 = 0.85, S_s^2 = 0.3, S^2 = S_f^2 S_s^2 = 0.255, \tau_s = 3$ ns and $\tau_f = 50$ ps. "Experimental" errors of 2.5% for the R_1 and R_2 rates and 5% for the ^{15}N–{^{1}H} NOE were assumed. Black circles represent the case where the NOE ratio at 700 MHz was overestimated and the correct value was used at 900 MHz, the reverse case is represented by gray circles. Filled circles represent cases where the correct model ($S^2, S_f^2, \tau_s, \tau_f$) was selected based on the relaxation rates using a statistical F-test while open circles represent cases where the incorrect model (S^2, S_f^2, τ_s only) was chosen. The dashed lines represent the correct motional parameters. The black concentric circles in (e) represent cases for which none of the possible dynamic models passed the goodness-of-fit test based on the corresponding χ^2 distribution. The χ^2 values for the most physical model in these cases have been displayed for illustration but the micro-dynamic parameters (which are erroneous) have not.

considered (Fig. 10) even though the average values of the fitted micro-dynamic parameters do not deviate significantly from the correct values. In extreme situations, for example, Fig. 10a–d, when the error in the NOE ratio exceeds 15% at 700 MHz (the correct value is used at 900 MHz) for an extended Lipari–Szabo model, the goodness-of-fit criterion is no longer satisfied and no motional model is found to be appropriate for the set of relaxation data and no micro-dynamic parameters can be obtained.

5. Conclusion

We have introduced a new scheme for the measurement of ^{15}N–$\{^{1}H\}$ NOE's. We have shown that this experiment provides a better estimate of the equilibrium polarization than previous approaches even for long recovery delays (8 s at 900 MHz). We show that the use of this new scheme with TROSY detection is likely to avoid systematic errors. For small proteins, the use of long recovery delays for the reference experiment should provide better precision. Systematic errors arising from the underestimation of the ^{15}N equilibrium polarization were shown to have variable impact on the parameters for local dynamics derived from a model-free approach. An improvement of the saturation schemes employed in the complementary experiment was introduced and evaluated through simulations. We are currently investigating in greater detail the nature of the saturation schemes utilized for ^{1}H saturation in the saturated experiment.

Appendix A

In this section, we present the expression of the Liouvillian superoperators used here for the simulation of the recovery of the spin system towards equilibrium. The spin system consists of one ^{15}N–^{1}H pair supplemented by two neighboring ^{1}H nuclei. One of these two ^{1}H nuclei shows enhanced auto-relaxation rates to take into account cross-relaxation or exchange with solvent protons during the recovery.

We have neglected all DD/DD cross-correlation mechanisms, as well as all long-range DD/CSA cross-correlations. We have not taken into account any cross-relaxation mechanism between neighboring ^{1}H nuclei and their ^{15}N partner. Under these conditions, we can restrict the basis of the subspace of the Liouville space to: $\{E/2, N_z, H_z, 2N_zH_z, H_z^I, 2N_zH_z^I, H_z^{II}, 2N_zH_z^{II}\}$. The Liouvillian superoperator is:

$$L_8 = \begin{pmatrix} 0 & 0 & 0 & 0 & 0 & 0 & 0 & 0 \\ \theta_N & \rho_N & \sigma_{NH} & \delta_N & 0 & 0 & 0 & 0 \\ \theta_H & \sigma_{NH} & \rho_H & \delta_H & \sigma_{HH} & 0 & \sigma_{HH} & 0 \\ \theta_{NH} & \delta_N & \delta_H & \rho_{NH} & 0 & \sigma_{HH} & 0 & \sigma_{HH} \\ \theta_H^I & 0 & \sigma_{HH} & 0 & \rho_H^I & \delta_N & 0 & 0 \\ \theta_{NH}^I & 0 & 0 & \sigma_{HH} & \delta_N & \rho_{NH}^I & 0 & 0 \\ \theta_H^{II} & 0 & 0 & \sigma_{HH} & 0 & 0 & \rho_H^{II} & \delta_N \\ \theta_{NH}^{II} & 0 & 0 & \sigma_{HH} & 0 & 0 & \delta_N & \rho_{NH}^{II} \end{pmatrix} \quad \text{(A1)}$$

where the expressions of the relaxation rates are:

$$\rho_N = \frac{1}{10}d_{NH}^2(3J(\omega_N) + J(\omega_N - \omega_H) + 6J(\omega_N + \omega_H)) + \frac{2}{15}d_N^2 J(\omega_N) \quad \text{(A2a)}$$

$$\rho_H = \frac{1}{10}d_{NH}^2(J(\omega_N - \omega_H) + 3J(\omega_H) + 6J(\omega_N + \omega_H))$$
$$+ \frac{2}{15}(d_{Hx} + d_{Hy})^2 J(\omega_H) + \frac{2}{10}d_{HH}^2(J(0) + 3J(\omega_H) + 6J(2\omega_H)) \quad \text{(A2b)}$$

$$\rho_{NH} = \frac{3}{10}d_{NH}^2(J(\omega_N) + J(\omega_H)) + \frac{2}{15}d_N^2 J(\omega_N) + \frac{2}{15}(d_{Hx} + d_{Hy})^2 J(\omega_H)$$
$$+ \frac{2}{10}d_{HH}^2(J(0) + 3J(\omega_H) + 6J(2\omega_H)) \quad \text{(A2c)}$$

$$\rho_H^I = \frac{1}{10}d_{NH}^2(J(\omega_N - \omega_H) + 3J(\omega_H) + 6J(\omega_N + \omega_H)) + \frac{2}{15}(d_{Hx} + d_{Hy})^2 J(\omega_H)$$
$$+ \frac{1}{10}d_{HH}^2(J(0) + 3J(\omega_H) + 6J(2\omega_H)) \quad \text{(A2d)}$$

$$\rho_{NH}^I = \frac{3}{10}d_{NH}^2(J(\omega_N) + J(\omega_H)) + \frac{2}{15}d_N^2 J(\omega_N) + \frac{2}{15}(d_{Hx} + d_{Hy})^2 J(\omega_H)$$
$$+ \frac{1}{10}d_{HH}^2(J(0) + 3J(\omega_H) + 6J(2\omega_H)) \quad \text{(A2e)}$$

$$\rho_H^{II} = \rho_H \quad \text{(A2f)}$$

$$\rho_{NH}^{II} = \rho_{NH} \quad \text{(A2g)}$$

$$\sigma_{NH} = \frac{1}{10}d_{NH}^2(6J(\omega_H + \omega_N) - J(\omega_H - \omega_N)) \quad \text{(A2h)}$$

$$\sigma_{HH} = \frac{1}{10}d_{HH}^2(6J(2\omega_H) - J(0)) \quad \text{(A2i)}$$

$$\delta_N = \frac{2}{5}d_{NH}d_N J_N(\omega_N) \quad \text{(A2j)}$$

$$\delta_H = \frac{1}{5}d_{NH}(d_{Hx}J_{Hx}(\omega_H) + d_{Hy}J_{Hy}(\omega_H)) \quad \text{(A2k)}$$

with: $d_{NH} = (\mu_0/4\pi)\hbar\gamma_N\gamma_H r_{NH}^{-3}; d_{HH} = (\mu_0/4\pi)\hbar\gamma_H^2 r_{HH}^{-3}; d_N = \omega_N\Delta\sigma_N;$ $d_{Hx} = \omega_H(\sigma_{Hxx} - \sigma_{Hzz}); d_{Hy} = \omega_H(\sigma_{Hyy} - \sigma_{Hzz}); \omega_N = -\gamma_N B_0; \omega_H = -\gamma_H B_0; \mu_0$ is the permittivity of free space; γ_N and γ_H are the gyromagnetic ratio of ^{15}N and hydrogen nuclei; r_{NH} is the distance between the ^{15}N nucleus and its neighboring ^{1}H nucleus; r_{HH} is the distance between two ^{1}H nuclei; $\Delta\sigma_N$ is the chemical shift anisotropy of the ^{15}N nucleus; $\sigma_{Hxx}, \sigma_{Hyy}$ and σ_{Hzz} are the three principal components of the ^{1}H chemical shift tensor; B_0 is the static magnetic field.

The spectral density functions employed make the assumption of uncorrelated isotropic local and global motions. A model-free form was employed for the case of local motions on one time scale.

$$J(\omega) = S^2 \frac{\tau_c}{1 + \omega^2\tau_c^2} + (1 - S^2)\frac{\tau_e}{1 + \omega^2\tau_e^2} \quad \text{(A3)}$$

where S^2 is the generalized order parameter, τ_c the correlation time for the overall tumbling time and τ_e is defined from the correlation time for local motions τ_{loc} by: $\tau_e^{-1} = \tau_c^{-1} + \tau_{loc}^{-1}$. The extended model-free form was used to describe the case of the motion of a small-domain in a large protein:

$$J(\omega) = S_s^2 \frac{\tau_c}{1 + \omega^2\tau_c^2} + (1 - S_f^2)\frac{\tau_{ef}}{1 + \omega^2\tau_{ef}^2} + (S_f^2 - S_s^2)\frac{\tau_{es}}{1 + \omega^2\tau_{es}^2} \quad \text{(A4)}$$

where S_s^2 and S_f^2 are the generalized order parameter for slow domain motions and fast local motions, respectively; the time constants τ_{es} and τ_{ef} are defined from the correlation times for slow domain τ_s and fast local τ_f motions by the relationships: $\tau_{es}^{-1} = \tau_c^{-1} + \tau_s^{-1}$ and $\tau_{ef}^{-1} = \tau_c^{-1} + \tau_f^{-1}$. Under isotropic global, domain and local motions, the spectral density functions for cross-correlated relaxation can be derived from auto-correlated spectral density functions by the relationship:

$$J_N(\omega) = \frac{3\cos^2(\theta_N) - 1}{2}J(\omega) \quad \text{(A5)}$$

$$J_{Hx}(\omega) = \frac{3\cos^2(\theta_{Hx}) - 1}{2}J(\omega) \quad \text{(A6a)}$$

$$J_{Hy}(\omega) = \frac{3\cos^2(\theta_{Hy}) - 1}{2}J(\omega) \quad \text{(A6b)}$$

where the angle θ_N describes the relative orientation of the NH vector and the principal axis of the axially symmetric ^{15}N chemical shift anisotropy tensor; θ_{Hx} and θ_{Hx} describe the relative orientation of the NH vector and the x and y principal axes of the ^1H CSA tensor, respectively.

The values employed for the above-mentioned parameters are: $r_{NH} = 101$ pm; $r_{HH} = 290$ pm; $\Delta\sigma_N = 164$ ppm; $\theta_N = 19°$; $\sigma_{Hxx} = 14.6$ ppm; $\sigma_{Hyy} = 8.2$ ppm; $\sigma_{Hzz} = 2.1$ ppm; $\theta_{Hx} = 90°$; $\theta_{Hy} = 99°$.

References

[1] A. Mittermaier, L.E. Kay, Review—New tools provide new insights in NMR studies of protein dynamics, Science 312 (2006) 224–228.

[2] A.G. Palmer III, NMR characterization of the dynamics of biomacromolecules, Chem. Rev. 104 (2004) 3623–3640.

[3] N. Tjandra, S.E. Feller, R.W. Pastor, A. Bax, Rotational diffusion anisotropy of human ubiquitin from N-15 NMR relaxation, J. Am. Chem. Soc. 117 (1995) 12562–12566.

[4] D. Fushman, N. Tjandra, D. Cowburn, An approach to direct determination of protein dynamics from 15N NMR relaxation at multiple fields, independent of variable 15N chemical shift anisotropy and chemical exchange contributions, J. Am. Chem. Soc. 121 (1999) 8577–8582.

[5] Y.E. Shapiro, E. Kahana, V. Tugarinov, Z.C. Liang, J.H. Freed, E. Meirovitch, Domain flexibility in ligand-free and inhibitor-bound *Escherichia coli* adenylate kinase based on a mode-coupling analysis of N-15 spin relaxation, Biochemistry 41 (2002) 6271–6281.

[6] N. Bloembergen, E.M. Purcell, R.V. Pound, Relaxation effects in nuclear magnetic resonance absorption, Phys. Rev. 73 (1948) 679–712.

[7] A. Abragam, Principles of Nuclear Magnetism, Oxford University Press, 1961.

[8] A.G. Redfield, Theory of relaxation processes, Adv. Magn. Reson. 1 (1965) 1–32.

[9] L.D. Favro, Theory of the rotational Brownian motion of a free rigid body, Phys. Rev. 119 (1960) 53–62.

[10] N.A. Farrow, O.W. Zhang, A. Szabo, D.A. Torchia, L.E. Kay, Spectral density-function mapping using N-15 relaxation data exclusively, J. Biomol. NMR 6 (1995) 153–162.

[11] S. Grzesiek, A. Bax, The Importance of not saturating H₂O in protein NMR—application to sensitivity enhancement and NOE measurements, J. Am. Chem. Soc. 115 (1993) 12593–12594.

[12] Q.G. Gong, R. Ishima, N-15-{H-1} NOE experiment at high magnetic field strengths, J. Biomol. NMR 37 (2007) 147–157.

[13] C. Renner, M. Schleicher, L. Moroder, T.A. Holak, Practical aspects of the 2D N-15-{H-1}-NOE experiment, J. Biomol. NMR 23 (2002) 23–33.

[14] N.J. Skelton, A.G. Palmer, M. Akke, J. Kordel, M. Rance, W.J. Chazin, Practical aspects of 2-dimensional proton-detected N-15 spin relaxation measurements, J. Magn. Reson. Ser. B 102 (1993) 253–264.

[15] M.H. Levitt, L. Di Bari, Steady-state in magnetic-resonance pulse experiments, Phys. Rev. Lett. 69 (1992) 3124–3127.

[16] R. Ghose, Average Liouvillian theory in nuclear magnetic resonance—principles, properties, and applications, Concepts Magn. Reson. 12 (2000) 152–172.

[17] P. Pelupessy, F. Ferrage, G. Bodenhausen, Accurate measurement of longitudinal cross-relaxation rates in nuclear magnetic resonance, J. Chem. Phys. 126 (2007) 134508.

[18] J. Jeener, Superoperators in magnetic-resonance, Adv. Magn. Reson. 10 (1982) 1–51.

[19] T.O. Levante, R.R. Ernst, Homogeneous versus inhomogeneous quantum-mechanical master-equations, Chem. Phys. Lett. 241 (1995) 73–78.

[20] G. Lipari, A. Szabo, Model-free approach to the interpretation of nuclear magnetic resonance relaxation in macromolecules 1. Theory and range of validity, J. Am. Chem. Soc. 104 (1982) 4546–4559.

[21] M. Goldman, Interference effects in the relaxation of a pair of unlike spin-1/2 nuclei, J. Magn. Reson. 60 (1984) 437–499.

[22] R. Ishima, D.A. Torchia, Extending the range of amide proton relaxation dispersion experiments in proteins using a constant-time relaxation-compensated CPMG approach, J. Biomol. NMR 25 (2003) 243–248.

[23] D.M. Korzhnev, P. Neudecker, A. Mittermaier, V.Y. Orekhov, L.E. Kay, Multiple-site exchange in proteins studied with a suite of six NMR relaxation dispersion experiments: an application to the folding of a Fyn SH3 domain mutant, 127 (2005) 15602–15609.

[24] C.D. Kroenke, J.P. Loria, L.K. Lee, M. Rance, A.G. Palmer III, Longitudinal and transverse H-1–N-15 dipolar N-15 chemical shift anisotropy relaxation interference: unambiguous determination of rotational diffusion tensors and chemical exchange effects in biological macromolecules, J. Am. Chem. Soc. 120 (1998) 7905–7915.

[25] K.H. Gardner, L.E. Kay, The use of H-2, C-13, N-15 multidimensional NMR to study the structure and dynamics of proteins, Annu. Rev. Biopys. Biomol. Struct. 27 (1998) 357–406.

[26] J.H. Chill, J.M. Louis, J.L. Baber, A. Bax, Measurement of N-15 relaxation in the detergent-solubilized tetrameric KcsA potassium channel, J. Biomol. NMR 36 (2006) 123–136.

[27] P.M. Hwang, N.R. Skrynnikov, L.E. Kay, Domain orientation in beta-cyclodextrin-loaded maltose binding protein: diffusion anisotropy measurements confirm the results of a dipolar coupling study, J. Biomol. NMR 20 (2001) 83–88.

[28] C.Y. Wang, M. Rance, A.G. Palmer, Mapping chemical exchange in proteins with $M_W > 50$ kDa, J. Am. Chem. Soc. 125 (2003) 8968–8969.

[29] M.D. Sorensen, A. Meissner, O.W. Sorensen, Spin-state-selective coherence transfer via intermediate states of two-spin coherence in IS spin systems: application to E.COSY-type measurement of J coupling constants, J. Biomol. NMR 10 (1997) 181–186.

[30] K. Pervushin, R. Riek, G. Wider, K. Wüthrich, Attenuated T-2 relaxation by mutual cancellation of dipole–dipole coupling and chemical shift anisotropy indicates an avenue to NMR structures of very large biological macromolecules in solution, Proc. Natl. Acad. Sci. USA 94 (1997) 12366–12371.

[31] K.V. Pervushin, G. Wider, K. Wüthrich, Single transition-to-single transition polarization transfer (ST2-PT) in [N-15,H-1]-TROSY, J. Biomol. NMR 12 (1998) 345–348.

[32] F. Ferrage, T.R. Eykyn, G. Bodenhausen, Highly selective excitation in biomolecular NMR by frequency-switched single-transition cross-polarization, J. Am. Chem. Soc. 124 (2002) 2076–2077.

[33] K. Pervushin, Impact of transverse relaxation optimized spectroscopy (TROSY) on NMR as a technique in structural biology, Q. Rev. Biophys. 33 (2000) 161–197.

[34] A.J. Shaka, C.J. Lee, A. Pines, Iterative schemes for bilinear operators—application to spin decoupling, J. Magn. Reson. 77 (1988) 274–293.

[35] K. Loth, P. Pelupessy, G. Bodenhausen, Chemical shift anisotropy tensors of carbonyl, nitrogen, and amide proton nuclei in proteins through cross-correlated relaxation in NMR spectroscopy, J. Am. Chem. Soc. 127 (2005) 6062–6068.

[36] G.M. Clore, A. Szabo, A. Bax, L.E. Kay, P.C. Driscoll, A.M. Gronenborn, Deviations from the simple 2-parameter model-free approach to the interpretation of N-15 nuclear magnetic-relaxation of proteins, J. Am. Chem. Soc. 112 (1990) 4989–4991.

[37] G. Zhu, Y.L. Xia, L.K. Nicholson, K.H. Sze, Protein dynamics measurements by TROSY-based NMR experiments, J. Magn. Reson. 143 (2000) 423–426.

[38] R. Ghose, D. Fushman, D. Cowburn, Determination of the rotational diffusion tensor of macromolecules in solution from NMR relaxation data with a combination of exact and approximate methods—application to the determination of interdomain orientation in multidomain proteins, J. Magn. Reson. 149 (2001) 204–217.

[39] D. Fushman, S. Cahill, D. Cowburn, The main chain dynamics of the dynamin pleckstrin homology (PH) domain in solution: analysis of 15N relaxation with monomer/dimer equilibration, J. Mol. Biol. 266 (1997) 173–194.